# Effect of beam current on defect formation by high-temperature implantation of Mg ions into GaN

Yuta Itoh[1], Hirotaka Watanabe[2], Yuto Ando[2], Emi Kano[2], Manato Deki[4], Shugo Nitta[2], Yoshio Honda[2], Atsushi Tanaka[2,3], Nobuyuki Ikarashi[2], and Hiroshi Amano[2,4,5]

[1]*Graduate School of Engineering, Nagoya University, Nagoya 464-8603, Japan*
[2]*Institute of Materials and Systems for Sustainability, Nagoya University, Nagoya 464-8601, Japan*
[3]*National Institute for Materials Science, Tsukuba 305-0044, Japan*
[4]*Venture Business Laboratory, Nagoya University, Nagoya 464-8603, Japan*
[5]*Akasaki Research Centre, Nagoya University, Nagoya 464-8603, Japan*
E-mail: ito.yuta@nagoya-u.jp

We evaluated the beam current dependence of defect formation during Mg ion implantation into GaN at a high temperature of 1100°C with two beam currents. Photoluminescence spectra suggest that low-beam-current implantation reduced the vacancy concentration and activated Mg to a greater extent. Moreover, scanning transmission electron microscopy analysis showed that low-beam-current implantation reduced the density of Mg segregation defects with inactive Mg and increased the density of intrinsic dislocation loops, suggesting decreases in the densities of Ga and N vacancies. The formation of these defects depended on beam current, which is an important parameter for defect suppression.

Gallium nitride (GaN) has a wide bandgap, high breakdown electric field, and high electron mobility.[1–3] To take advantage of its excellent physical properties, GaN is applied to the fabrication of power devices such as metal-oxide-semiconductor field-effect transistors and the edge termination structure.[4–10] These devices require ion implantation (I/I) to form localized n-type and p-type regions. However, the fabrication of p-type Mg-ion-implanted GaN remains a challenge. Recently, the demonstration of p-type conductivity and the temperature-dependent Hall effect measurement have been reported with annealing above 1400°C at a nitrogen pressure of 1 GPa.[11–14] They have indeed been breakthroughs; however, for the practical implementation of novel devices, the ambient-pressure fabrication is desirable because there are strict regulations in the use of high-pressure and high-temperature systems in many countries.

Defect control in I/I is essential in fabricating p-type Mg-ion-implanted GaN at ambient pressure. It has been reported that many primary defects, such as vacancies and interstitials, are formed during I/I, and that annealing to remove them results in the formation of various secondary defects.

For instance, positron annihilation spectroscopy studies indicated that Mg I/I generates a high concentration of the Ga and N vacancy complex ($V_{Ga}V_N$).[15,16] During annealing above 1000°C, these vacancies begin to agglomerate and form vacancy clusters that act as carrier traps, such as $(V_{Ga})_3(V_N)_3$. Moreover, the implanted Mg ions segregated above the concentration of $1\times10^{19}$ cm$^{-3}$, indicating a high concentration of inactive Mg.[17] Thus, the formation of secondary defects, such as vacancy clusters and Mg segregation defects must be suppressed to obtain high p-type conductivity.

To resolve these issues, we propose a technique of I/I at a high temperature (HT). In this HT-I/I technique, primary defects are expected to be annihilated either by their instantaneous return to the original site or diffusion to the surface without forming secondary defects. Previously, the dependence of implanted ion concentration on annealing temperature was reported.[18–24] In particular, the results of HT-I/I above 1000°C suggested the activation effect of Mg and the suppression of defect formation compared with conventional I/I without intentional heating.[18] If HT-I/I can suppress defect formation, beam current should be an important parameter because it is expressed as the number of defects introduced per unit time. Therefore, low-beam-current implantation should lead to more defects being removed by annealing during heating. In this study, we performed HT-I/I with different beam currents of two orders of magnitude and evaluated the dependence of defect formation on beam current.

Mg ions were implanted into unintentionally doped (UID) Ga-polar GaN grown on a free-standing GaN substrate. UID-GaN of 3 μm thickness was grown by metalorganic vapor phase epitaxy (MOVPE). Impurities such as carbon, oxygen, and silicon are at background levels or lower than $10^{16}$ cm$^{-3}$. As a protective film during HT-I/I, a 50-nm-thick AlN layer was deposited by MOCVD at 500°C on both sides. Mg ions were implanted at energies of 100 and 40 keV with the corresponding doses of $1.3\times10^{14}$ and $2.8\times10^{13}$ cm$^{-2}$, respectively. A sharp box-shaped profile with a depth of 100 nm was formed at a Mg concentration of $1.0\times10^{19}$ cm$^{-3}$. The angles of the samples were set to 7 and 15° from the c- and m-axes, respectively, to prevent channeling. The temperature during implantation was 1100°C, which was monitored using a thermocouple set on the surface of the sample. A sample was placed on a carbon susceptor and heated by infrared irradiation from the back surface. The beam current was set to 100 and 1 μA. In our implantation device, a pulse of ions was applied for 0.06 ms over a period of 3.25 ms. Beam current densities of 100 and 1 μA were obtained as 31.83 and 0.318 μAcm$^{-2}$, respectively. The implantation duration was set to 68 and 6,800 s for 100 and 1 μA, respectively, to keep the total dose constant. To regulate the thermal annealing of 100 and 1 μA as-implanted samples, 100 μA as-implanted samples were annealed in vacuum at 1100°C for 6,732 s. These samples are referred to as 100 μA+heated, and the other two samples as 1 and 100 μA as-implanted. After removing the AlN protective film, a 100-nm-thick AlN protective film for post annealing was again deposited. All the samples were annealed at 1250°C for 45 s in $N_2$ gas at atmospheric pressure. In this paper, we denote the samples obtained after HT-I/I and annealing at

1250°C for 45 s as "as-implanted" and "post-annealed", respectively. To evaluate the effect of beam current on defect formation, we determined the luminescence characteristics and analyzed the defects by using scanning transmission electron microscopy (STEM).

Figures 1(a) and 1(b) show the results of secondary ion mass spectrometry of as-implanted and post-annealed samples, respectively. Compared with the 100 μA and 100 μA+heated as-implanted samples, the Mg concentration of the 1 μA as-implanted sample decreased at a depth of around 100 nm and increased at depths larger than 200 nm owing to diffusion. Furthermore, post annealing reduced the Mg concentration peak around 50 nm; the Mg ions in the reduced peak may have diffused to the surface. These Mg diffusion behaviors are clearly dependent on the beam current, which may be due to the different density and type of defects formed by 1 μA and 100 μA implantation.

We determined the luminescence characteristics of as-implanted and post-annealed samples by photoluminescence (PL) measurement at 77 K. A 325 nm He–Cd laser was utilized at an excitation density of 260 $Wcm^{-2}$. The luminescence characteristics observed at 77 K are as follows. The high intensity of near-band-edge (NBE) emission at around 3.47 eV suggests a decrease in the concentration of nonradiative recombination centers (NRCs).[25] The donor–acceptor-pair (DAP) emission at around 3.28 eV suggests the activation of Mg. The green luminescence (GL) at around 2.35 eV is characteristic of Mg-ion-implanted GaN, and the GL is identified as GL2.[25-27] The origin of GL2 is attributed to the formation of N vacancies ($V_N$s),[26,27] which we also assume in our discussion. The PL spectra of as-implanted and post-annealed samples are shown in Figs. 2(a) and 2(d), respectively. The DAP, NBE, their LO replicas, and GL2 were clearly observed in all the samples.

In as-implanted samples [Fig. 2(a)], the GL2 intensities of the 1 and 100 μA samples were almost the same but it was about twice as high as that of the 100 μA+heated sample. The 100 μA+heated sample was annealed for another 6,732 s after the implantation, whereas heating of the 100 and 1 μA samples was stopped as soon as the implantation was completed. Thus, some areas of the 1 and 100 μA samples are amorphous, and their GL2 intensities were lower than that of the 100 μA+heated sample. The DAP intensity of the 1 μA sample was higher than that of the 100 μA sample but comparable to that of the 100 μA+heated sample. As in the case of GL2, the Mg ions introduced into the last batch should not have been activated. The NBE intensity of the 1 μA sample was the highest among all the samples, and the NBE intensities of the other two samples were comparable. The evaluation of the as-implanted samples did not show that implantation at 1 μA was particularly superior to that at 100 μA in terms of both GL2 and DAP intensities. However, a clearly higher NBE intensity indicated that Mg could be implanted with fewer defects formed at the same dose.

In the case of post-annealed samples [Fig. 2(d)], the GL2 intensity of the 1 μA sample was lower than those of the 100 μA and 100 μA+heated samples. These suggest that $V_N$s formation was suppressed during post annealing since low-beam-current implantation decreased the $V_N$ concentration in the as-implanted samples. The DAP and NBE intensities of the 1 μA sample was sufficiently higher

than those of the 100 μA and 100 μA+heated samples. It is clear that implantation at 1 μA contributed to the increases in DAP and NBE intensities, indicating the further activation of Mg and the decrease in the concentration of $V_{Ga}$ complexed with $V_N$s, which act as NRCs. These results showed that the intensities of GL2, DAP, and NBE clearly depended on the beam current, not on the total annealing time, and low-beam-current implantation is more effective than high-beam-current implantation in further activating Mg and reducing the vacancy concentration.

To investigate the beam current dependence of the structural properties, we analyzed the defects by annular dark-field scanning transmission electron microscopy (ADF-STEM). The ADF-STEM cross-sectional images of as-implanted and post-annealed samples are shown in Figs. 3(a)–(c) and 3(d)–(f), respectively. In this experiment, extended defects appearing as bright dots and loops were observed. Bright dots were observed in all the samples and bright loops in post-annealed samples. We investigated the characteristics of bright dots and loops by STEM and high-angle ADF (HAADF-STEM) analyses.

Figure 4(a) shows an HAADF-STEM image of the extended defects indicated by a solid triangle in Fig. 3(c). A triangular contrast, which has an upper (0001) facet and (11-23) side facets, can be observed. The energy-dispersive X-ray spectroscopy (EDS) spectrum of the (0001) facet in the red rectangle is shown in Fig. 4(b). This spectrum shows that the Mg concentration increased around the boundary of (0001), indicating that the triangular defects have a high concentration of Mg. A similar defect is confirmed in p-type GaN grown epitaxially by doping with a high concentration of Mg.[17,28] Structurally, it is a pyramidal inversion domain (PID) with a high concentration of inactive Mg at the (0001) facet and inhibits p-type conductivity. The triangular defects have features in common with the PID, indicating that the PID-like Mg segregation defects also have a high concentration of inactive Mg.

We utilized an inside–outside technique to identify whether the bright circles are extrinsic or intrinsic dislocation loops by following the procedure described in ref. 29. We confirmed that the bright circles were intrinsic dislocation loops. Such defects have been observed in Mg-implanted GaN after UHPA at 1300℃ for more than 30 min or at 1400℃ for more than 5 min and after Mg segregation defects had disappeared.[29,30]

We converted the number of these defects into areal density in the c-axis direction and examined the effects of low-beam-current implantation, by comparing with the PL spectrum. Table I shows the defect densities of as-implanted and post-annealed samples. The low-beam-current implantation such as that at 1 μA significantly decreased the density of extended defects, which implies a decrease in the density of vacancies and interstitial atoms. Some of the extended defects are PID-like Mg segregation defects with inactive Mg; the fewer the PID-like Mg segregation defects, the greater the extent of Mg being activated. In addition, the number of intrinsic dislocation loops increased, and since the loops are formed by vacancy aggregation,[29] vacancies probably disappeared.

These support the PL results suggesting a decrease in the density of vacancies and a higher activation of Mg by low-beam-current implantation. Thus, the evaluations of PL and STEM indicate that low-beam-current implantation reduces the defect density and further activates Mg. There are several considerations from the perspective of secondary defect formation and beam current. The density of primary defects formed by low-beam-current implantation is the same as that formed by high-beam-current implantation, but the density of defects formed per unit time is lower. Furthermore, at a high temperature, some of the formed primary defects should disappear owing to their diffusion to the surface or annihilation. Therefore, we consider that the low density of primary defects per unit time leads to the reduction of the probability of aggregation with other primary defects, and more primary defects diffuse to the surface or are instantly annihilated.

In summary, we performed the HT-I/I of Mg into GaN with two beam currents. PL spectra suggest that the reduction in beam current suppressed the vacancy concentration and activated Mg to a greater extent. From the results of STEM analyses, the areal density of extended defects including PID-like Mg segregation defects decreased and that of dislocation loops increased with the reduction in the beam current. These results support the idea that low-beam-current implantation suppresses the formation of vacancies and that the post annealing further activates Mg. We consider that the control of the beam current can lower the annealing temperature and shorten the annealing time for p-type Mg-implanted GaN.

## Acknowledgments

This work was supported by MEXT-Program for Creation of Innovative Core Technology for Power Electronics Grant Number JPJ009777.

## References


1) T. Maeda, T. Narita, S. Yamada, T. Kachi, T. Kimoto, M. Horita, and J. Suda, J. Appl. Phys. **129**, 185702 (2021).
2) H. Fujikura, T. Konno, T. Kimura, Y. Narita, and F. Horikiri, Appl. Phys. Lett. **117**, 012103 (2020).
3) T. Narita, K. Tomita, Y. Tokuda, T. Kogiso, M. Horita, and T. Kachi, J. Appl. Phys. **124**, 215701 (2018).
4) R. Tanaka, S. Takashima, K. Ueno, H. Matsuyama, M. Edo, and K. Nakagawa, Appl. Phys. Express **12**, 054001 (2019).
5) R. Tanaka, S. Takashima, K. Ueno, H. Matsuyama, and M. Edo, Jpn. J. Appl. Phys. **59**, SGGD02 (2020).
6) M. Yoshino, Y. Ando, M. Deki, T. Toyabe, K. Kuriyama, Y. Honda, T. Nishimura, H. Amano, T. Kachi, T. Nakamura, Materials **12**, 689 (2019).
7) M. Matys, T. Ishida, K. Pil Nam, H. Sakurai, K. Kataoka, T. Narita, T. Uesugi, M. Bockowski, T. Nishimura, Jun Suda, Appl. Phys. Express **14**, 074002 (2021).
8) M. Matys, T. Ishida, K. Pil Nam, H. Sakurai, T. Narita, T. Uesugi, M. Bockowski, J. Suda, and T. Kachi, Appl. Phys. Lett. **118**, 093502 (2021).
9) J. R. Dickerson, A. A. Allerman, B. N. Bryant, A. J. Fischer, M. P. King, M. W. Moseley, A. M. Armstrong, R. J. Kaplar, I. C. Kizilyalli, O. Aktas, and J. J. Wierer, IEEE Trans. Electron Devices **63**, 419 (2016).
10) T. J. Anderson, J. D. Greenlee, B. N. Feigelson, J. K. Hite, F. J. Kub and K. D. Hobart, ECS J. Solid State Sci. Technol. **5**, Q176 (2016).
11) H. Sakurai, M. Omori, S. Yamada, Y. Furukawa, H. Suzuki, T. Narita, K. Kataoka, M. Horita, M. Bockowski, J. Suda, and T. Kachi, Appl. Phys. Lett. **115**, 142104 (2019).
12) H. Sakurai, T. Narita, M. Omori, S. Yamada, A. Koura, M. Iwinska, K. Kataoka, M. Horita, N. Ikarashi, M. Bockowski, J. Suda, and T. Kachi, Appl. Phys. Express **13**, 086501 (2020).
13) K. Sierakowski, R. Jakiela, B. Lucznik, P. Kwiatkowski, M. Iwinska, M. Turek, H. Sakurai, T. Kachi, and M. Bockowski, Electronics **9**, 1380 (2020).
14) M. H. Breckenridge, J. Tweedie, P. Reddy, Y. Guan, P. Bagheri, D. Szymanski, S. Mita, K. Sierakowski, M. Bockowski, R. Collazo, and Z. Sitar, Appl. Phys. Lett. **118**, 022101 (2021).
15) A. Uedono, S. Takashima, M. Edo, K. Ueno, H. Matsuyama, H. Kudo, H. Naramoto, and S. Ishibashi, Phys. Status Solidi B **252**, 2794 (2015).
16) A. Uedono, S. Takashima, M. Edo, K. Ueno, H. Matsuyama, W. Egger, T. Koschine, C. Hugenschmidt, M. Dickmann, K. Kojima, S. F. Chichibu, S. Ishibashi, Phys. Status Solidi B **255**, 1700521 (2018).
17) A. Kumar, W. Yi, J. Uzuhashi, T. Ohkubo, J. Chen, T. Sekiguchi, R. Tanaka, S. Takashima, M. Edo, and K. Hono, J. Appl. Phys. **128**, 065701 (2020).

18) M. Takahashi, A. Tanaka, Y. Ando, H. Watanabe, M. Deki, M. Kushimoto, S. Nitta, Y. Honda, K. Shima, K. Kojima, S. F. Chichibu, and H. Amano, Jpn. J. Appl. Phys. **59**, 056502 (2020).
19) A. Wenzel, C. Liu, and B. Rauschenbach, Mater. Sci. Eng. B **59**, 191 (1999).
20) S. Whelan, M. J. Kelly, R. Gwilliam, C. Jeynes, and C. Bongiorno, J. Appl. Phys. **98**, 013515 (2005).
21) A. Lardeau-Falcy, M. Coig, M. Charles, C. Licitra, J. Kanyandekwe, F. Milési, J. Eymery, and F. Mazen, ECS Trans. **80**, 131 (2017).
22) T. Niwa, T. Fujii, and T. Oka, Appl. Phys. Express **10**, 091002 (2017).
23) A. Kumar, K. Mitsuishi, T. Hara, K. Kimoto, Y. Irokawa, T. Nabatame, S. Takashima, K. Ueno, M. Edo, and Y. Koide, Nanoscale Res. Lett. **13**, 403 (2018).
24) M. Sumiya, K. Fukuda, S. Takashima, S. Ueda, T. Onuma, T. Yamaguchi, T. Honda, and A. Uedono, J. Cryst. Growth **511**, 15 (2019).
25) S. F. Chichibu, K. Shima, K. Kojima, S. Takashima, K. Ueno, M. Edo, H. Iguchi, T. Narita, K, Kataoka, S. Ishibashi and A. Uedono, Jpn. J. Appl. Phys. **58**, SC0802 (2019).
26) K. Kojima, S. Takashima, A. Edo, K. Ueno, M. Shimizu, T. Takahashi, S. Ishibashi, A. Uedono, and S. F. Chichibu, Appl. Phys. Express **10**, 061002 (2017).
27) M. A. Reshchikov, D. O. Demchenko, J. D. McNamara, S. Fernández-Garrido, and R. Calarco, Phys. Rev. B **90**, 035207 (2014).
28) T. Narita, N. Ikarashi, K. Tomita, K. Kataoka, and T. Kachi, J. Appl. Phys. **124**, 165706 (2018).
29) K. Iwata, H. Sakurai, S. Arai, T. Nakashima, T. Narita, K. Kataoka, M. Bockowski, M. Nagao, J. Suda, T. Kachi, and N. Ikarashi, J. Appl. Phys. **127**, 105106 (2020).
30) T. Nakashima, E. Kano, K. Kataoka, S. Arai, H. Sakurai, T. Narita, K. Sierakowski, M. Bockowski, M. Nagao, J. Suda, T. Kachi and N. Ikarashi, Appl. Phys. Express **14**, 011005(2021).

## Figure captions

**Fig. 1.** (Color online) Depth profiles of Mg in (a) as-implanted samples and (b) post-annealed samples. (annealed at 1250°C for 45 s)

**Fig. 2.** (Color online) PL spectra at 77 K for (a) as-implanted samples. (b)–(c) PL intensity axis on a linear scale of (a). (d) PL spectra for post-annealed samples. (e)–(f) PL intensity axis on a linear scale of (d)

**Fig. 3.** Cross-sectional ADF-STEM images of (a) 100 μA as-implanted sample, (b) 100 μA+heated as-implanted sample, (c) 1 μA as-implanted sample, (d) 100 μA post-annealed sample, (e) 100 μA+heated post-annealed sample, and (f) 1 μA post-annealed sample.

**Fig. 4.** (a) HAADF-STEM image of Mg segregation defect. (b) EDS spectra measured at the (0001) facet of the triangle (red rectangle) and the GaN matrix.

**Table I.** Areal density in the c-axis direction of as-implanted and post-annealed sample. All densities are calculated in the arrowed area of Fig. 3(a)

| Sample name | Extended defect ($\times 10^{10}$ cm$^{-2}$) | Dislocation loop ($\times 10^{10}$ cm$^{-2}$) |
|---|---|---|
| 100 μA | 13.70 / 13.50 | 0.00 / 0.23 |
| 100 μA+heated | 11.05 / 12.05 | 0.00 / 0.32 |
| 1 μA | 3.02 / 2.36 | 0.00 / 0.54 |

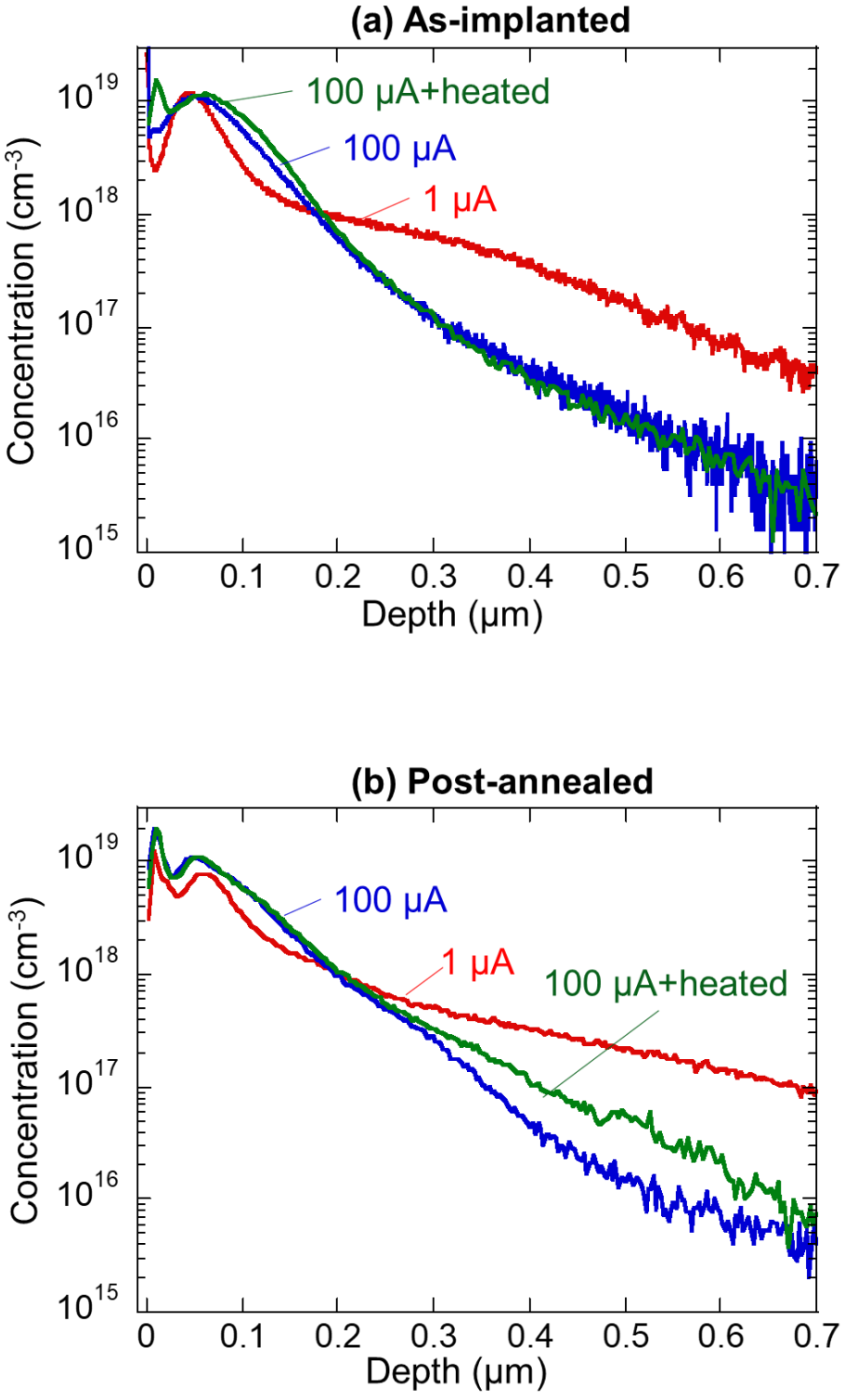
(a) As-implanted
100 μA+heated
100 μA
1 μA
Concentration (cm-3)
Depth (μm)
(b) Post-annealed
100 μA
1 μA
100 μA+heated
Concentration (cm-3)
Depth (μm)

Fig. 1.

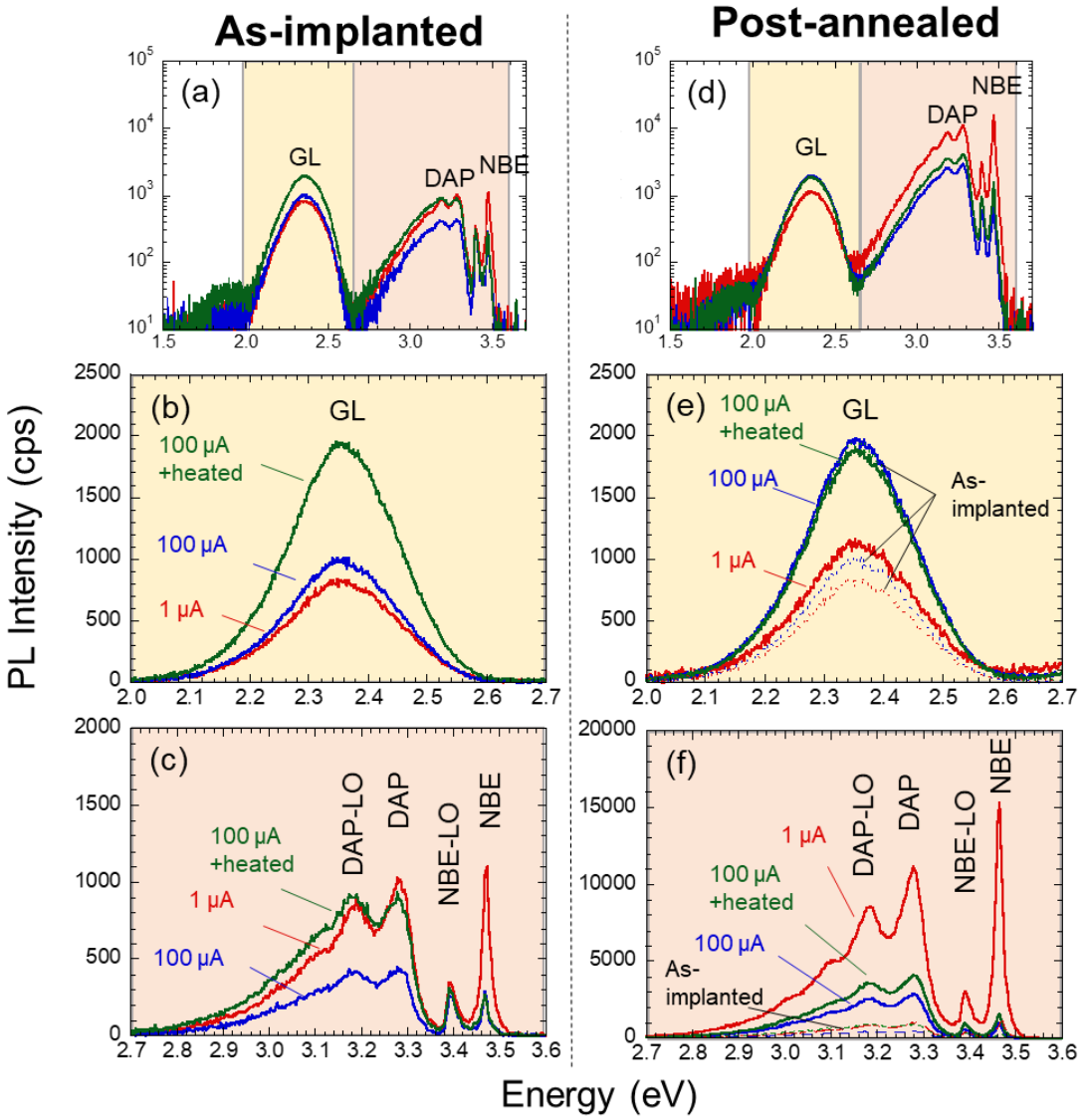
As-implanted
Post-annealed
(a)
GL
DAP
NBE
(d)
GL
DAP
NBE
(b)
GL
100 μA
+heated
100 μA
1 μA
(e)
GL
100 μA
+heated
100 μA
1 μA
As-
implanted
(c)
DAP-LO
DAP
NBE-LO
NBE
100 μA
+heated
1 μA
100 μA
(f)
DAP-LO
DAP
NBE-LO
NBE
1 μA
100 μA
+heated
100 μA
As-
implanted
PL Intensity (cps)
Energy (eV)

Fig. 2.

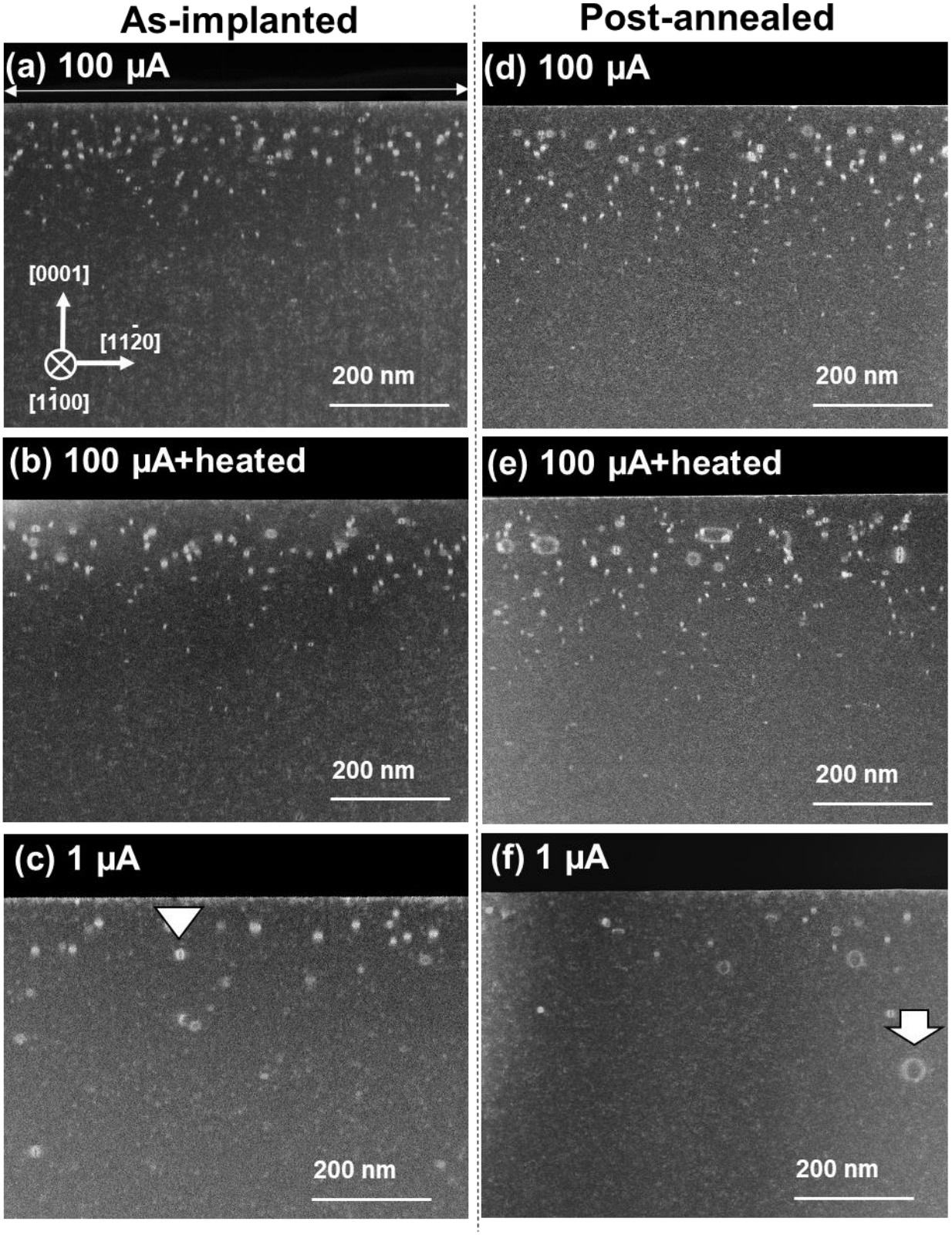
As-implanted
Post-annealed
(a) 100 μA
(d) 100 μA
[0001]
[11$\bar{2}$0]
[1$\bar{1}$00]
200 nm
200 nm
(b) 100 μA+heated
(e) 100 μA+heated
200 nm
200 nm
(c) 1 μA
(f) 1 μA
200 nm
200 nm

Fig. 3.

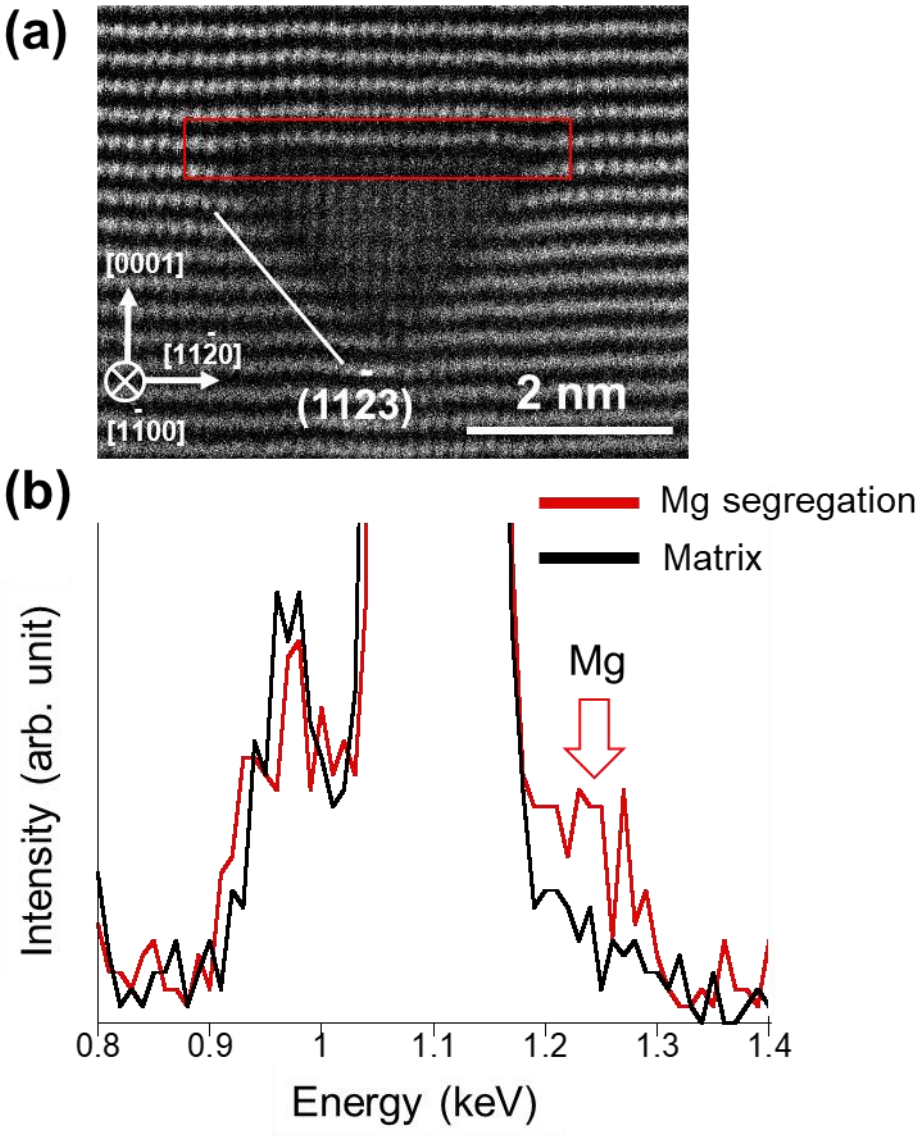
(a)
[0001]
[11$\bar{2}$0]
[1$\bar{1}$00]
(11$\bar{2}$3)
2 nm
(b)
Mg segregation
Matrix
Mg
Intensity (arb. unit)
0.8
0.9
1
1.1
1.2
1.3
1.4
Energy (keV)

Fig. 4.